A Section 508–conformant HTML version of this article is available at https://doi.org/10.1289/EHP4927.

Evaluation of the Nose-to-Brain Transport of Different Physicochemical Forms of Uranium after Exposure *via* Inhalation of a UO_4 Aerosol in the Rat

Chrystelle Ibanez,[1] David Suhard,[2] Christelle Elie,[1] Teni Ebrahimian,[1] Philippe Lestaevel,[1] Audrey Roynette,[3] Bernadette Dhieux-Lestaevel,[3] François Gensdarmes,[3] Karine Tack,[1] and Christine Tessier[4]

[1]Institut de Radioprotection et de Sûreté Nucléaire, Pôle Santé Environnement, Service de recherche sur les effets biologiques et sanitaires des rayonnements ionisants, Laboratoire de Radiotoxicologie et Radiobiologie Expérimentale, Fontenay aux Roses, France
[2]Institut de Radioprotection et de Sûreté Nucléaire, Pôle Santé Environnement, Service de recherche sur les effets biologiques et sanitaires des rayonnements ionisants, Laboratoire de Recherche en Radiochimie, Spéciation et Imagerie, Fontenay aux Roses, France
[3]Institut de Radioprotection et de Sûreté Nucléaire, Pôle de Sûreté des Installations et des Systèmes Nucléaire, Service du Confinement et de l'Aérodispersion des Polluants, Laboratoire de Physique et de Métrologie des Aérosols, Gif-sur-Yvette, France
[4]Institut de Radioprotection et de Sûreté Nucléaire, Fontenay aux Roses, France

Background: Health-risk issues are raised concerning inhalation of particulate pollutants that are thought to have potential hazardous effects on the central nervous system. The brain is presented as a direct target of particulate matter (PM) exposure because of the nose-to-brain pathway involvement. The main cause of contamination in nuclear occupational activities is related to exposure to aerosols containing radionuclides, particularly uranium dust. It has been previously demonstrated that instilled solubilized uranium in the rat nasal cavity is conveyed to the brain via the olfactory nerve.

Objective: The aim of this study was to analyze the anatomical localization of uranium compounds in the olfactory system after *in vivo* exposure to a polydisperse aerosol of uranium tetraoxide (UO_4) particles.

Methods: The olfactory neuroepithelium (OE) and selected brain structures—olfactory bulbs (OB), frontal cortex (FC), hippocampus (HIP), cerebellum (Cer), and brainstem (BS)—were microdissected 4 h after aerosol inhalation *via* a nose-only system in adult rats. Tissues were subjected to complementary analytical techniques.

Results: Uranium concentrations measured by inductively coupled plasma mass spectrometry (ICP-MS) were significantly higher in all brain structures from exposed animals compared with their respective controls. We observed that cerebral uranium concentrations followed an anteroposterior gradient with typical accumulation in the OB, characteristic of a direct olfactory transfer of inhaled compounds. Secondary ion mass spectrometry (SIMS) microscopy and transmission electron microscopy coupled with energy-dispersive X-ray spectroscopy (TEM-EDX) were used in order to track elemental uranium *in situ* in the olfactory epithelium. Elemental uranium was detected in precise anatomical regions: olfactory neuron dendrites, paracellular junctions of neuroepithelial cells, and olfactory nerve tracts (around axons and endoneural spaces).

Conclusion: These neuroanatomical observations in a rat model are consistent with the transport of elemental uranium in different physicochemical forms (solubilized, nanoparticles) along olfactory nerve bundles after inhalation of UO_4 microparticles. This work contributes to knowledge of the mechanistic actions of particulate pollutants on the brain. https://doi.org/10.1289/EHP4927

Introduction

The association between exposure to particulate pollutants *via* inhalation and the increased risk of deleterious effects on the central nervous system is an emerging issue. Numerous experimental and epidemiological studies have focused on the biological effects of particulate matter (PM) on the respiratory and cardiovascular systems, and there is now growing evidence that the brain could be a direct target after exposure *via* inhalation (Heusinkveld et al. 2016; Oberdörster et al. 2009). The potential deleterious effect of PM inhalation is relevant to the global population, in part because of the many pathways for exposure and, PM, for instance, is widely mentioned in relationship to environmental exposure due to traffic-related air pollution.

The literature (including *in vitro, in vivo* animal, and epidemiological studies) describes solid observations of the negative impact of PM on neurological functions (Lucchini et al. 2012). Several studies have focused on the biological effects on the brain of air pollution in large urban areas. An epidemiological study has suggested that long-term exposure to traffic-related air pollution could be an important risk factor for vascular dementia and Alzheimer's disease in a major city in northern Sweden (Oudin et al. 2016). Studies of selected canine subjects [7 dogs from Mexico City compared with 14 dogs from another city with lower air pollution (Calderón-Garcidueñas et al. 2008)] and postmortem analyses in children [9 children from Mexico City compared with 6 children from another city with lower air pollution; (Calderón-Garcidueñas et al. 2016)] point to a trigger of a neuroinflammation process in the brain of exposed dogs and humans (Block and Calderón-Garcidueñas 2009). Postmortem analyses of Mexican children exposed to high air pollution showed white matter lesions in the prefrontal cortex (Calderón-Garcidueñas et al. 2016). These observations were extended last year by experimental rodent studies suggesting direct effects of PM on the neuroinflammation process, in particular, prenatal exposure to diesel exhaust (DE) particles in microglial cell activation in male mice (Bolton et al. 2017), an effect of ammonium sulfate exposure on neuronal maturation in adult male mice (Cheng et al. 2017), and exposure to nanoscale PM in neuronal atrophy in young female mice (Woodward et al. 2017). Neuroinflammation appears to be the first trigger of the central effects of PM (Jayaraj et al. 2017).

Health risks associated with exposure *via* particle inhalation may also be encountered in specific occupational activities. In nuclear facilities, contaminations are mainly caused by airborne PM, i.e., particularly aerosols in mines and during nuclear fuel cycle operations, and nuclear dismantling represents a potential hazard for exposed workers (Anderson et al. 2016; Samson et al.

Address correspondence to Dr. Chrystelle Ibanez, IRSN/PSE-SANTE/SESANE, LRTOX, BP17, 92262 Fontenay aux Roses Cedex, France. Telephone: +33 (0) 1 58 35 82 84. Fax: +33 (0) 1 58 35 84 67. Email: chrystelle.ibanez@irsn.fr

The authors declare that they have no actual or potential competing financial interests.

Received 20 December 2018; Revised 26 July 2019; Accepted 13 August 2019; Published 30 September 2019.

Note to readers with disabilities: *EHP* strives to ensure that all journal content is accessible to all readers. However, some figures and Supplemental Material published in *EHP* articles may not conform to 508 standards due to the complexity of the information being presented. If you need assistance accessing journal content, please contact ehponline@niehs.nih.gov. Our staff will work with you to assess and meet your accessibility needs within 3 working days.

2016). We believe that the latter operations will become more and more frequent in the future and are the cause of radioactive particle resuspension or direct emission (Chae et al. 2019; Peillon et al. 2017). Aerosols contain particles ranging in size (micrometric to nanometric) and chemical composition, including dust containing uranium particles [mainly uranium oxide particles].

The involvement of the nose-to-brain pathway is suggested by Lucchini et al. (2012) and Oberdörster et al. (2004), and the latter refers to cerebral effects of inhaled ultrafine particles in rat models.

In 2016, Maher et al. illustrated the extent to which the olfactory system is a strong link between the external environment and the central nervous system, as they observed magnetite particles of exogenous origin in the human brain (Maher et al. 2016). The literature also suggests the involvement of the olfactory pathway for other metals: mercury (Henriksson and Tjalve 1998), cobalt (Persson et al. 2003), and cadmium (Bondier et al. 2008) after nasal instillation or nebulization, and for ultrafine manganese oxide particles after inhalation (Elder et al. 2006).

With regard to uranium, pilot studies strongly suggest that it can be transferred to the brain in rats exposed to repeated depleted uranium oxide aerosol inhalation (uranium oxide powder is depleted in ^{235}U as compared with natural uranium). In an inductively coupled plasma mass spectrometry (ICP-MS) analysis, Monleau et al. (2005) revealed that elemental uranium accumulated in the olfactory bulbs (OB) of male rats, even though the final physicochemical form was not studied (Monleau et al. 2005). Subsequently, Tournier et al. (2009) confirmed a uranium anteroposterior gradient in the brains of male rats after inhalation, and proposed a direct role of the olfactory neurons in its transfer (Tournier et al. 2009). Our recent study has strengthened this hypothesis. We demonstrated, using secondary ion mass spectrometry (SIMS) microscopy, uranium transport along olfactory nerve bundles of male rats and delivery to the brain *via* the cerebrospinal fluid after intranasal instillation of depleted uranium (Ibanez et al. 2014).

The concern in terms of potential neurotoxicity of uranium after exposure *via* aerosol inhalation is linked to its dual toxicity: chemical, as it is a heavy metal, and radiotoxicity, due to its radioactivity. It will also be important to consider the influence of the physicochemical changes of uranium particles on the subsequent biological effects and mechanisms of transport to the brain (solubilized compounds, nanoparticles, and ion forms). For instance, different physicochemical forms of cerium dioxide nanoparticles induce differential toxicity responses in rodents after inhalation (Dekkers et al. 2018). In the inhalation mode of exposure, one study demonstrated that uranium-exposed male rats exhibited poorer performance in spatial working memory tests than did control rats (Monleau et al. 2005). These experiments raise concerns in terms of cognitive impairments provoked by inhalation of aerosolized uranium particles. In terms of radioprotection, biological contamination follow-up is based on biokinetic models that have been developed to predict uranium distribution in the main body compartments, particularly after contamination by inhalation (ICRP 1994). However, these models do not take into account the potential existence of direct transfer of uranium to the brain via the olfactory pathway (ICRP 1994).

We thus decided to continue our previous investigations using a model of inhalation exposure to uranium tetraoxide (UO_4) particles. The aim of this study was to provide robust anatomical evidence of the localization of elemental uranium in the olfactory system after exposure of adult male rats to UO_4 aerosol *via* nose-only inhalation. These experiments complement the observations made using the intranasal administration model with an aqueous solution containing solubilized uranium (Ibanez et al. 2014). A precise definition of elemental uranium distribution after exposure to the uranium particulate form will provide evidence for the existence of a specific uranium olfactory route.

Adult male rats were exposed to a polydisperse aerosol of UO_4 using nose-only inhalation chambers. Elemental uranium concentrations resulting from these exposures were measured by ICP-MS in different brain structures along the anteroposterior axis of the brain: olfactory bulb (OB), frontal cortex (FC), hippocampus (HIP), cerebellum (Cer), and brainstem (BS). In order to detect *in situ* localization of solubilized and particulate forms of uranium in the olfactory neuroepithelium (OE), we used two different high-resolution microscopy techniques: SIMS microscopy, a very sensitive surface analysis technique able to map uranium distribution in tissue sections, and transmission electron microscopy coupled with energy-dispersive X-ray spectroscopy (TEM-EDX), which provides detection at a nanoscale dimension and characterizes chemical elements.

Methods

Animals

Adult male Sprague-Dawley rats (12 wk old) from Charles River Laboratories were used for all experiments. Animals were housed in the IRSN (Institut de Radioprotection et de Sûreté Nucléaire) animal facilities accredited by the French Ministry of Agriculture. Food and water were provided *ad libitum* (lights on: 0800 to 2000 hours; temperature: $22°C \pm 1°C$; humidity: $55\% \pm 10\%$). Experimental groups were designed as follows: a combined control group and two exposed groups in two different series, series 1 and series 2, exposed at different aerosol concentrations, as described in the next section. Twenty-four animals were used for uranium concentration analysis by ICP-MS ($n = 8$ per group: one control group and two exposed groups, series 1 and series 2). Eighteen animals were used for uranium *in situ* localization using high-resolution microscopy ($n = 6$ per group: control group and 2 exposed groups, series 1 and 2). Animal experiments were performed in compliance with French and European regulations on protection of animals used for scientific purposes (EC Directive 2010/63/EU and French Decree 2013–118). They were approved by Ethics Committee #81 and authorized by the French Ministry of Research (reference 01017.01).

Aerosol Generation and Inhalation Procedure

UO_4 powder (Orano NC) is depleted in ^{235}U as compared with natural uranium, and it contains the nonnatural ^{236}U isotope. The isotopic composition by mass of the UO_4 powder was isotope 238 of uranium $^{238}U = 99.55\%$, $^{236}U = 0.051\%$; $^{235}U = 0.39\%$, and $^{234}U = 0.0047\%$.

The nose-only inhalation system and the procedure have been previously described (Tournier et al. 2009). Our inhalation glove box is made of three parts: the aerosol generator chamber containing a rotating brush generator (RBG 1000; Palas) used for aerosol generation from dry powder. The nose-only tubes are connected to the aerosol exposure chamber. The outlet of the RBG 1000 is directly connected to the top of the exposure chamber by antistatic tubing. The chamber is equipped with high-efficiency exhaust filters in order to prevent contamination of the glove box. The noses of the rats were in direct contact with aerosols in the exposure chamber connected with the nose-only tubes. The third part contains the devices used to perform aerosol metrology. An Aerodynamic Particle Sizer® (APS™ Spectrometer 3321; TSI) combined with a diluter was used to determine particle size distribution and for real-time monitoring of the aerosol concentration in the inhalation chamber. The reference aerosol concentration in the inhalation chamber was measured by

sampling particles on cellulose acetate membrane filters (0.8 μm pore size, 25 mm diameter; Millipore) with a constant flow rate equal to 2 L/min. The uranium mass concentration was determined by weight and ICP-MS analysis.

Before exposure *via* inhalation, all animals were progressively acclimatized to the tubes over a period of 3 wk in order to avoid the stress induced by the inhalation procedure (three progressive sessions per week: the first session duration was 10 min, and length was incremented by 10 min at each session to reach 1 h, which included the total length of the procedure, inhalation exposure, and transfer inside the glove box). Rats were exposed to uranium aerosols for 30 min. Control rats were also maintained in tubes and exposed to ambient air for 30 min. All animals were euthanized 4 h after the end of inhalation, and selected tissues were collected. Two different aerosol concentrations were selected in order to increase the chance of being above the detection limits of the imaging techniques used in our study. Our previous studies provided us robust feedback on the minimal exposure concentrations that could be detected without affecting the ultrastructure of the olfactory epithelium (Tournier et al. 2009; Ibanez et al. 2014). The mean aerosol concentrations during exposure were 218 mg/m^3 for series 1 and 545 mg/m^3 for series 2. The series 2 exposure concentration is within the range found in our previous work (Monleau et al. 2005, Tournier et al. 2009). The aim was also to expose animals to a lower (half) concentration in series 1. The aerodynamic mass median diameter was 4.6 μm for series 1 and 4.4 μm for series 2.

Aerosol size distribution was also characterized by TEM analysis and image processing. To perform image processing and particle size distribution analysis, we used the advanced software provided with the Morphologi G3 instrument (Malvern Panalytical) (Malvern, version 7). The aerosol sample analyzed was collected directly on the TEM grids and deposited at the surface of the filter used for mass concentration measurement. Results are described in Figure 1.

Sample Collection and Inductively Coupled Plasma Mass Spectrometry Analysis (ICP-MS)

Rats were deeply anesthetized by inhalation of 5% isoflurane and 95% air and sacrificed by exsanguination 4 h after inhalation. This time point was based on the study performed with the intranasal instillation model (Ibanez et al. 2014), and it coincides with a peak of accumulation of uranium in the brain after nasal exposure in rodent models (Ibanez et al. 2014; Petitot et al. 2013). The OE was dissected out, weighed, and stored at −80°C. Selected brain structures were microdissected after the brain was removed and placed on ice: OB, FC, HIP, Cer, and BS. As for OE, samples were weighed and stored at −80°C. In order to measure uranium concentration, samples were first dissolved in 8 mL of 69% nitric acid HNO_3 (Aristar®; VWR) and 2 mL of 30% hydrogen peroxide (NORMAPUR®; VWR) using a microwave oven (Ethos Start D Microwave Digestion System 1000 W; Milestone). The nitric acid digestion mixture was warmed to 180°C over 15 min and then held for a further 10 min at the same temperature in the microwave oven at 1,000 W using the digestion rotor system. Samples were then evaporated on heating plates under a fume hood and dissolved in 3 mL of 20% HNO_3. All samples from each different brain structure were diluted appropriately (1/10) and analyzed for elemental uranium concentration using an ICP-MS (X series II, Thermo Electron with S-Option; Thermo Fisher Scientific). Bismuth was used as the internal standard (Claritas PPT Grade, catalog number: SPEX CertiPrep™ CLBI2-1AY, purity: 97.99%, 10 mg/L in 2% HNO_3; Fisher Scientific). The quantification limit of uranium measured by ICP-MS was 1 ng/L for ^{238}U and ^{235}U.

Biological Sample Preparation for Secondary Ion Mass Spectrometry (SIMS) Microscopy and Transmission Electron Microscopy Coupled with Energy-Dispersive X-ray Spectroscopy (TEM-EDX) Analysis

Olfactory neuroepithelia were dissected out 4 h after inhalation as described previously, and the tissue was submitted for a standard chemical fixation procedure. Samples were fixed with a solution containing 2.5% glutaraldehyde for 1 h at room temperature, dehydrated in ethanol baths, and permeabilized with a propylene oxide/Epon mixture. No osmium or uranyl acetate was used to counterstain the tissue samples in order to avoid artefacts for both the SIMS and TEM-EDX observations and analyses. This procedure allowed the olfactory epithelium sections to be observed in their physiological state. Finally, samples were embedded in pure Epon-type resin (Electron Microscopy Sciences, ref 14900, Hatfield TA19440). Serial transverse thin sections (900 nm) embedded in resin were cut and laid on polished ultrapure silicon holders for SIMS analysis (to avoid relief effects and minimize charge effects), or on glass slides and stained with toluidine blue for histological controls with an optical microscope. Ultrathin transverse sections (70 nm) were cut and collected on copper grids for TEMS.

Secondary Ion Mass Spectrometry (SIMS) Microscopy

The aim of SIMS microscopy is the elemental and isotopic analysis of a solid surface by an ion beam coupled with a mass spectrometer. This technique is based upon the sputtering of a few atomic layers from the surface of a sample, induced by the bombardment of focused primary ions (O_2^+, O^-, Cs^+, or Ar^+) with sufficiently high energy [several kiloelectron volts (KeV)]. These primary ions penetrate the solid surface and transfer some of their kinetic energy to the target particles, creating collision cascades that induce the emission of surface particles (atoms or molecules) in a charged or uncharged state. The secondary ions are representative of the elemental and isotopic composition of the bombarded analyzed area. They are accelerated and analyzed with a mass spectrometer (electrostatic sector and magnetic sector) on the basis of the mass-to-charge ratio. The sputtered ions stemming from each point of the bombarded surface are focused into an image by an immersion objective lens. The SIMS analysis was performed using a CAMECA IMS 4F E7 instrument. For this study, O^{2+} beam bombardment was used to enhance the ionization field of electropositive species such as uranium [Energy (E) = 12 KeV; Intensity (I) = 500 picoampere (pA)]. In this scanning microscope, the primary beam was focused into a small shaft (around 0.5 μm), which scans the sample surface. The collected secondary ions were measured with an electron multiplier and also sequentially converted into an image. Mass resolution could reach 10,000 ($M/\Delta M$), and the lateral resolution of the imaging was 0.5 μm. For each area analyzed, mass spectra at around the mass of ^{238}U and ion images were obtained. $^{23}Na^+$ images gave the histological structure of the sample, and $^{238}U^+$ images showed uranium fixation within the structures. Analyses were performed as follows: two controls, two animals of series 1, and five animals of series 2 were analyzed. For each animal, an average of 10 areas (200 × 200 μm) were fully mapped for $^{23}Na^+$ and $^{238}U^+$.

Transmission Electron Microscopy Coupled With Energy-Dispersive X-ray Spectroscopy (TEM-EDX) Analysis

Compared with light microscopy, TEM uses an electron beam instead of light, thus providing optimal resolution and revealing the finest details of an internal structure at high magnification, here within the olfactory mucosa. The condenser lens of the microscope allows restriction of the electron beam into a thin and

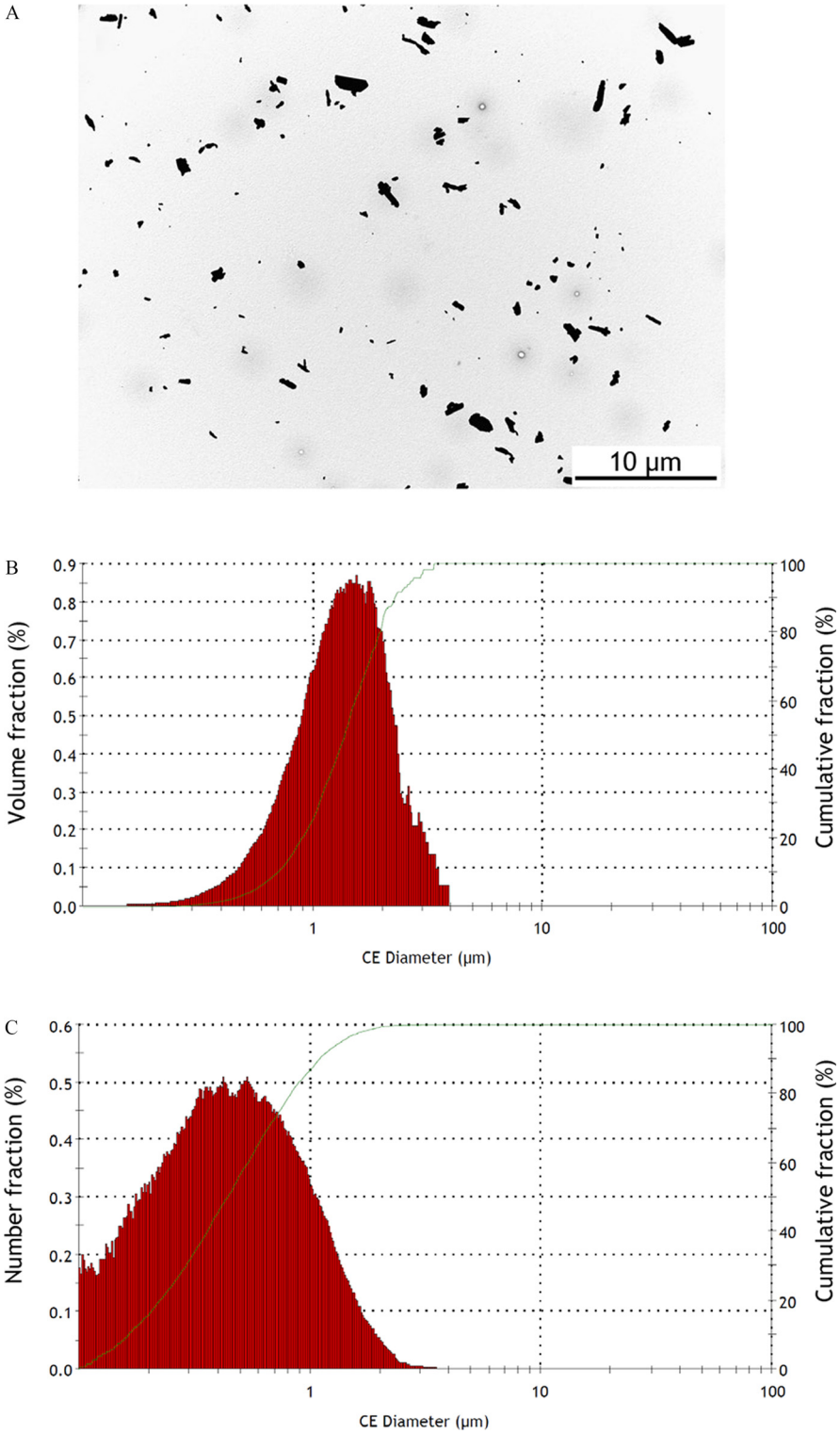

Figure 1. Transmission electron microscopy (TEM) microphotograph and particle size distributions in uranium tetraoxide (UO_4) aerosol. (A) Representative TEM microphotograph of UO_4 particle (scale bar: 10 µm). (B) Particle volume size distribution. (C) Particle count size distribution. The particle size distribution from the particle image processing is expressed according to the circumference-equivalent diameter (CE diameter) of particles. (B) Shows the CE diameter size distribution in terms of particle volume (calculated from CE diameter). Results show a median CE diameter equal to 1.4 µm with a volume size distribution spread between 0.1 µm and 4 µm [red bars represent the volume fraction (%), green line graph represents the cumulative fraction (%)]. (C) Represents the distribution of CE diameter according to particle number. The count median diameter was equal to 0.4 µm and the size distribution obtained revealed that, in terms of number, 90% of particles had a CE diameter below 1 µm [red bars represent the number fraction (%); green line graph represents the cumulative fraction (%)].

coherent beam by modulating its aperture. The beam then strikes the ultrathin sections collected on a grid. The resulting image on the charge-coupled device (CCD) camera depends upon the thickness and electron transparency of the tissue section. The contrast can be modulated using high-angle diffracted electrons and projector lenses, which allow the image to be focused and enlarged. Dark areas in the image correspond to areas where few electrons are transmitted and lighter areas where more electrons can go through the specimen. The power of the electron beam is expressed in KeV. In our study, the ultrastructure observations of the olfactory mucosa ultrathin sections were performed using the Electron Microscopy Platform at the Muséum National d'Histoire Naturelle. The high-resolution transmission electron microscope used was the following: HT7700 model, 120 kV (Hitachi) with its associated STEM (scanning TEM) module and CCD camera. The aim of TEM microscopy is to provide precise ultrastructural cytoarchitecture of the olfactory epithelium. Because nanoscale particle detection has a restricted detection limit, analyses were then focused on animals exhibiting the relative higher concentration of uranium (as seen in SIMS analysis spectra). They were performed as follows: two controls and three animals of series 2 were analyzed. For each animal, an average of 4 TEM grids with 2 to 3 sections on each grid were observed under the microscope, resulting in an average of 10 sections analyzed per animal.

The elemental composition of the particles detected in our ultrathin sections of the olfactory mucosa was then analyzed with an EDX module. The principle of the EDX analysis relies on an electron beam that strikes the specimen within a selected area. This action results in the production of X-rays having the specific energies of the chemical elements present on the analyzed surface. The electron microscope is combined with an EDX detector (Thermo Fisher Scientific). EDX analysis was performed at 80 kV, and specific uranium energies were revealed for M and Lα (M and L refers to the name of atomic layers) at 3.1 and 13.6 KeV.

Statistical Analysis

Results from the ICP-MS measurements are expressed as mean $\pm$ standard deviation (SD). Nonparametric statistics were chosen to analyze ICP-MS results as the normality test (Shapiro-Wilk test) failed ($p < 0.05$). Uranium concentrations in the exposed groups were compared with the control for each brain structure using a Kruskal-Wallis one-way analysis of variance (ANOVA) on ranks, followed by a Mann-Whitney rank-sum test to compare each uranium condition with the control. The Kruskal-Wallis test was also performed to test if uranium concentration variations between the selected brain structures within the same group were different (Table 1; Figure 2). The level of significance was established for $p \leq 0.05$. In addition, statistical analysis using the Poisson distribution was performed in order to estimate the probability of detection of UO_4 particles of 0.5 µm and 1 µm diameter in a given tissue volume of the neuroepithelium analyzed by use of SIMS microscopy.

Table 1. Uranium concentrations in selected brain structures as measured by inductively coupled plasma mass spectrometry (ICP-MS).

	Uranium concentrations (ng/g tissue)		
Structures	Control	Series 1	Series 2
OB	1.51 ± 0.19	17.95 ± 13.34	15.31 ± 4.60
FC	2.01 ± 0.43	7.44 ± 1.89	12.33 ± 2.17
HIP	1.21 ± 0.08	4.70 ± 1.00	9.31 ± 3.15
Cer	0.47 ± 0.05	2.45 ± 0.47	5.25 ± 1.09
BS	0.87 ± 0.12	3.86 ± 0.59	8.25 ± 2.32

Note: Data are expressed as mean $\pm$ SD (Experimental groups: a combined control group and 2 exposed groups, series 1 and series 2, exposed at 218 mg/m^3 and 545 mg/m^3, respectively; $n = 8$ per group). BS, brainstem; Cer, cerebellum; FC, frontal cortex; HIP, hippocampus; OB, olfactory bulbs.

Results

Aerosol Metrology

Aerosol size distribution was characterized using the advanced software provided with the Morphologi G3 instrument. Results are reported in Figure 1. Figure 1A shows a typical TEM microphotograph of UO_4 particles analyzed by image processing. The particle size distribution from the particle image processing is expressed according to the circumference-equivalent diameter (CE diameter) of particles. This is the diameter of the disc with the same circumference of the particle. One should note that the CE diameter is distinct from the aerodynamic diameter, which determines the behavior of particles when airborne and also lung deposition. Figure 1B shows the CE diameter size distribution in terms of particle volume (calculated from the CE diameter). Results showed a median CE diameter equal to 1.4 µm with a volume size distribution spread between 0.1 and 4 µm. According to the different diagnostics used to track uranium in this study (mass of uranium by ICP-MS, uranium particle count by SIMS or TEM images), and due to the fact that particle size distribution is polydisperse, it was also relevant to characterize the size distribution according to particle number. The results obtained are depicted in Figure 1C, which represents the distribution of CE diameters according to particle number. The count median diameter was equal to 0.4 µm, and the size distribution obtained revealed that in terms of number, 90% of particles had a CE diameter below 1 µm. Due to constraints on the configuration of the microscope associated with the Morphologi G3 instrument at the time of the inhalation experiments, it was not possible to measure aerosol samples for particle sizes <100 nm. Nevertheless, it was possible to fit a lognormal function to the particle size distribution measured in Figure 1C and to assess, by calculation, the fraction of nanoparticles with a diameter <100 nm. Considering a count median diameter equal to 0.4 µm and a geometric SD of 2, giving the best fit, the particle fraction <100 nm was equal to 2%.

Quantification of Uranium Concentrations in Brain Structures

Adult male Sprague-Dawley rats were exposed to a polydisperse aerosol of UO_4 particles *via* a nose-only inhalation system and euthanized 4 h after the end of the exposure. Elemental uranium concentrations measured in selected brain structures were shown to be related to olfactory transport of metals after nasal exposure in rodents (Henriksson and Tjalve 1998; Ibanez et al. 2014; Persson et al. 2003; Tournier et al. 2009). Structures were dissected out along the anteroposterior axis of the brain: OB, FC, HIP, Cer, and BS. Results are presented in Table 1 for each group and structure as mean $\pm$ SD. Statistical analyses are presented in Figure 2. Comparisons were made between the control group and the two exposed groups (series 1 and 2) for each brain structure using nonparametric one-way ANOVA followed by a Mann-Whitney rank-sum test. Results revealed that uranium concentrations were higher for each structure from exposed animals from series 1 and 2 compared with their anatomically equivalent control structure (nonparametric ANOVA $^{***}p \leq 0.001$; Mann-Whitney $^{***}p \leq 0.001$ for each structure from series 1 and 2 compared with control). In addition, ICP-MS analysis of the isotopic ratio confirmed that elemental uranium, measured in the exposed animals, originated from our UO_4 powder depleted in ^{235}U (isotopic ratio was expressed as the percentage in ^{235}U and was 0.7% in the control group and 0.4% in both exposed groups).

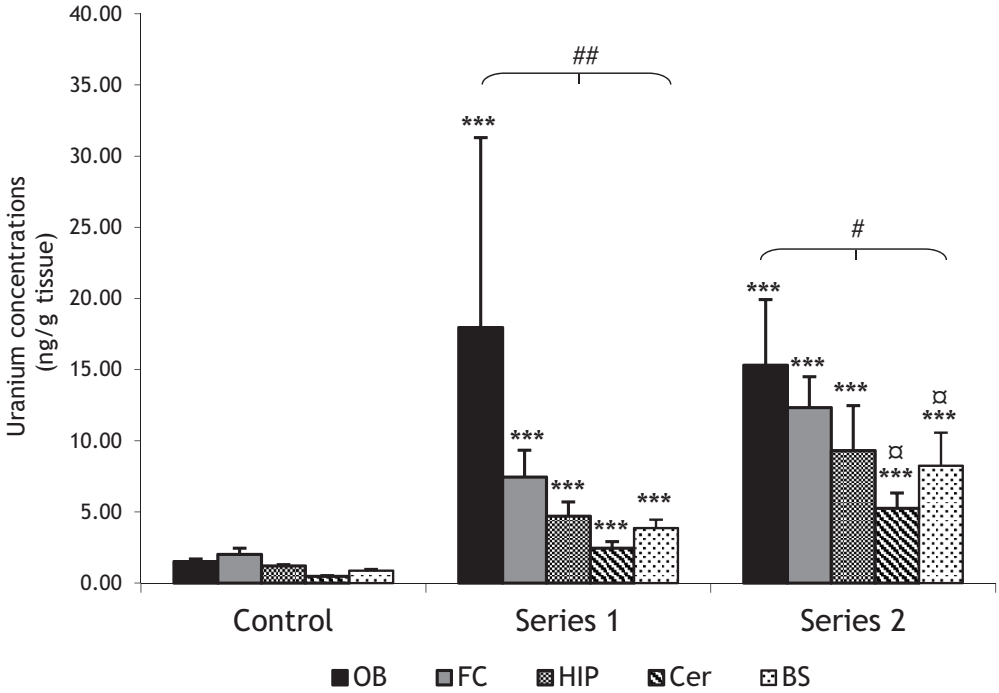

Figure 2. Statistical analysis comparing uranium concentrations in selected brain structures. Results are presented for adult male Sprague-Dawley rats exposed to a uranium tetraoxide (UO_4) aerosol *via* inhalation, and samples were collected 4 h after the end of the exposure ($n=8$ per group: a control group and two exposed groups; series 1 and 2). Data are expressed as mean + standard deviation (SD). *, significant difference between a control brain structure and its anatomical counterpart in the control group from the series 1 or 2 exposed groups [nonparametric analysis of variance (ANOVA) $^{***}p \leq 0.001$ followed by Mann-Whitney $^{***}p \leq 0.001$ for each structure compared with controls). #, significant difference between brain structures from a given group as determined by a nonparametric ANOVA, $^{\#\#}p=0.004$ for series 1 and $^{\#}p=0.027$ for series 2. ¤, significant difference between equivalent brain structures from series 1 and 2 as determined by a Mann-Whitney test; Cer: $^{¤}p=0.015$; BS: $^{¤}p=0.038$). Note: OB, olfactory bulbs; FC, frontal cortex; HIP, hippocampus; Cer, cerebellum; BS, brainstem.

In exposed groups from series 1 and 2, statistically significant frontal accumulation of uranium after inhalation was also revealed, as OB uranium concentrations were higher compared with the other brain structures, whereas uranium concentration was homogeneous in control animals. Animals exhibited significantly and progressively lower levels of uranium along the anteroposterior axis of the brain following the OB, FC, HIP, Cer, and BS structures (nonparametric ANOVA, $^{\#\#}p=0.004$ for series 1 and $^{\#}p=0.027$ for series 2).

Additional statistical analyses were performed to compare elemental uranium concentrations in equivalent brain structures in both exposed groups. OB, FC, and HIP uranium concentrations from series 1 and 2 were not statistically different from each other, but uranium concentrations were significantly higher in series 2 than in series 1 when Cer and BS structures were compared (¤Mann-Whitney test: Cer series 2 higher than Cer series 1, $^{¤}p=0.015$; BS series 2 higher than BS series 1, $^{¤}p=0.038$).

Uranium in Situ *Detection Using Secondary Ion Mass Spectrometry Microscopy in the Olfactory Mucosa*

In situ localization was performed to detect uranium in the olfactory neuroepithelium (OE) following exposure. The OE tissues were not counterstained with osmium or uranyl acetate in order to avoid artefacts in the detection of uranium.

Figure 3A represents the mass spectra of control and uranium-exposed animals from series 1 and 2 recorded at around the mass of ^{238}U at a low mass resolution ($M/\Delta M=300$). The mass spectra of the control did not show the presence of a significant peak at mass 238 above the background level. This result demonstrated that natural uranium was not detected by SIMS, and no polyatomic ions were superimposed on the element of interest at a low mass resolution. In that context, it was not essential to work at a high mass resolution. It was then decided to work at a low mass resolution, which improved secondary ion transmission and, therefore, the detection limits as well. In these conditions, the peak at mass 238 observed in the uranium-exposed animal resulted from the exposure via inhalation. The relative intensities between series 1 and 2 spectra are correlated to the aerosol concentrations.

Thin sections of the OE were counterstained with toluidine blue to obtain the neuroanatomical architecture and reference points for further microscopic analysis. The subsequent section was kept for SIMS analysis. Figure 3B shows a transverse section of the olfactory mucosa, with its different compartments: the Ne contains the olfactory receptor neuron (ORN) cell bodies located on the surface of the mucosa, together with supporting cells and neuronal progenitors. The basal lamina separates the neuroepithelium (Ne) from the lamina propria (LP) and represents an olfactory stem cell niche rich in extracellular matrix. The LP is a large compartment containing Bowman's gland cells and blood vessels. Within the LP are the olfactory nerve bundles in which the axons of the olfactory neurons converge (Ax). The nasal septum can also be observed on this section, supporting the different compartments of the nasal mucosa on each side of the nostrils.

Figure 3C represents the superimposed ionic $^{238}U^{+}$ (red) and $^{23}Na^{+}$ (green) images. On this image, uranium distribution was detected in the olfactory mucosa and appeared to be region specific. The higher uranium concentration was found on the surface

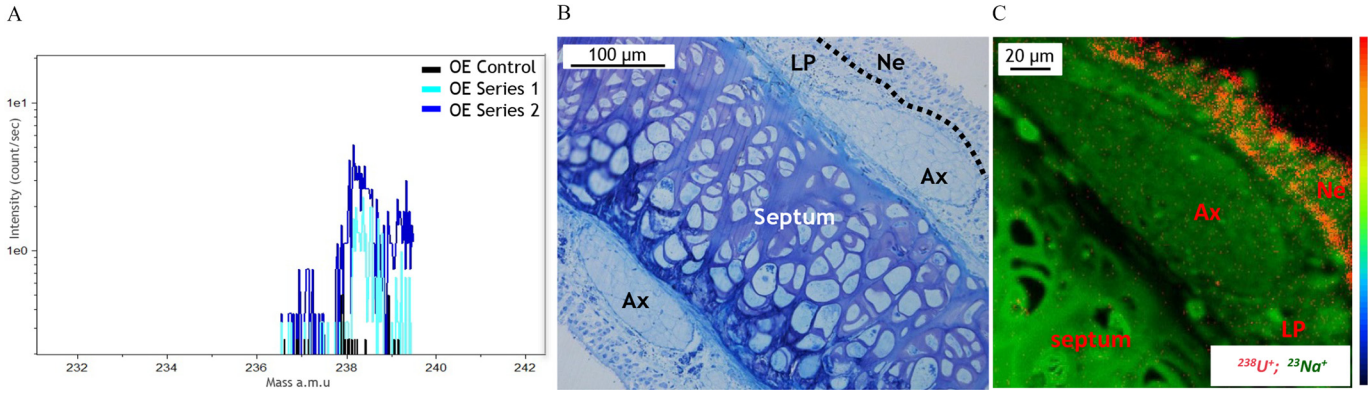

Figure 3. Secondary ion mass spectrometry (SIMS) analysis in the olfactory mucosa. Results are presented for adult male Sprague-Dawley rats exposed to a uranium tetraoxide (UO_4) aerosol *via* inhalation, and samples were collected 4 h after the end of the exposure ($n=6$ per group: one control group and two exposed groups, series 1 and 2). Analyses were performed as follows: two controls, two animals of series 1, and five animals of series 2 were analyzed. For each animal, an average of 10 areas (200 × 200 µm) were fully mapped for $^{23}Na^+$ and $^{238}U^+$. (A) Mass spectra of a control and contaminated rats via inhalation. The mass spectrum of the control remains at the background level, whereas a peak at mass 238 was observed in the uranium-exposed animal. OE, olfactory epithelium. (B) Optical toluidine blue microphotograph of the olfactory mucosa (scale bar: 100 µm). (C) SIMS microphotograph representing a serial section of (B) in the olfactory mucosa of an animal exposed to the UO_4 aerosol *via* inhalation (scale bar: 20 µm). It represents superimposed ionic images of $^{238}U^+$ (red) and $^{23}Na^+$ (green). The higher uranium concentration was found specifically in the Ne compartment. Uranium was not detected or was present but under the detection limit of the SIMS technology in the LP compartment or around the axon bundles. These results are from an animal from series 2, and are representative of exposed groups, as anatomical detection of uranium was similar in all sections analyzed for animals of series 1 and 2 (2 out of 2 animals from series 1, and 5 out of 5 animals from series 2). Ax, axon bundles; LP, lamina propria; Ne, neuroepithelium.

of the mucosa, specifically in the Ne compartment, which was in direct contact with aerosolized uranium particles at the time of the inhalation procedures. In the LP compartment and olfactory nerve bundle layer, particularly around the axon bundles, uranium was not detected, or rather was present but under the detection limit of the SIMS technology. These results are from an animal from series 2 and are representative of exposed groups, as anatomical detection of uranium was similar in all areas analyzed for animals of series 1 and 2, regardless of aerosol concentration (2 out of 2 animals from series 1, and 5 out of 5 animals from series 2).

In addition, considering the 0.5-µm size detection limit of SIMS microscopy, we aimed to estimate the probability of detection of UO_4 particles of 0.5 µm or 1 µm diameter in the analyzed tissue volume of the neuroepithelium using Poisson distribution. To make the probability calculation, several parameters were considered: UO_4 density and uranium mass fraction in UO_4. To proceed to the Poisson law calculation, we considered that all uranium concentrations measured by ICP-MS analysis in the OE corresponded to UO_4 particulate matter with a defined diameter (0.5 µm or 1 µm). Probabilities were calculated for the total volume represented by 10 different slices analyzed for exposed animal groups. Statistical analysis revealed that, in those conditions, we had a probability of 62.1% of finding one or more 0.5 µm particles. This probability was only 11.4% if we considered that all particles had a 1 µm diameter. It should be noted that the probability for a 0.5-µm-particle diameter was the most relevant, as it was close to the median diameter of the aerosol size distribution (0.4 µm). In consequence, we could not exclude that there might be some micron-sized particles in our neuroepithelial tissue.

Uranium in Situ *Detection Using Transmission Electron Microscopy Coupled with Energy-Dispersive X-ray Spectroscopy Analysis in the Olfactory Mucosa*

TEM analysis was undertaken in order to complement the SIMS observations made on animals from series 1 and 2. The rationale and aim of this analysis were based on our hypothesis that uranium could take different forms according to particle solubility in biological fluids and that this required both types of microscopy. For TEM analysis, OE tissues were not counterstained with osmium or uranyl acetate in order to avoid artefacts in the detection of uranium particles. Figure 4 represents a panel of optical and TEM microphotographs that were taken in different anatomical areas of the OE of adult male rats exposed to a polydisperse aerosol of UO_4 particles *via* inhalation, and euthanized 4 h after the end of exposure. The transverse section of the olfactory mucosa with its different compartments stained with toluidine blue is shown in Figure 4A. Neuroanatomical reference points between the anatomical zones illustrated in Figure 4A and the TEM microphotographs at much higher magnification in Figure 4B–F are indicated with solid- or hatched-line squares in Figure 4A. Microphotographs in Figure 4B–D represent an olfactory axon bundle with endoneurium anatomical structures (Endo.) that can be easily recognized because of the presence of collagen fibers. Microphotographs in Figure 4C,D were taken successively at higher magnifications, and the imaged areas were indicated by large hatched-line squares in Figure 4A. Electron-dense objects were observed inside the axon bundles. When magnification was increased in the axon bundles shown in Figure 4C,D, these dense objects took on a nanoscale dimension, as observed in the microphotograph in Figure 4D with a scale bar set at 165 nm. These nanoscale objects tended to surround the axons rather than being inside them in the bundles. Other anatomical areas were investigated. The microphotograph in Figure 4E shows an electron-dense nanoparticle closely in contact with ORN dendrites at the surface of the Ne (solid-line square). The microphotograph in Figure 4F delineated by the dotted square shows the presence of nanoscale electron-dense matter in a paracellular junction in between two cells of the neuroepithelial compartment. These observations are representative of exposed groups, as the anatomical localization of electron-dense particles was similar in all sections analyzed for animals of series 2 (three out of three animals). Control animals did not exhibit electron-dense nanoparticles in any areas of the olfactory mucosa (data not shown).

The next objective was the elemental characterization of these nanoscale particles observed in the animals exposed to uranium *via* inhalation. EDX analysis was performed on the electron-dense particles that were observed in the anatomical areas illustrated in Figure 4. Results of these analyses are presented in Figure 5.

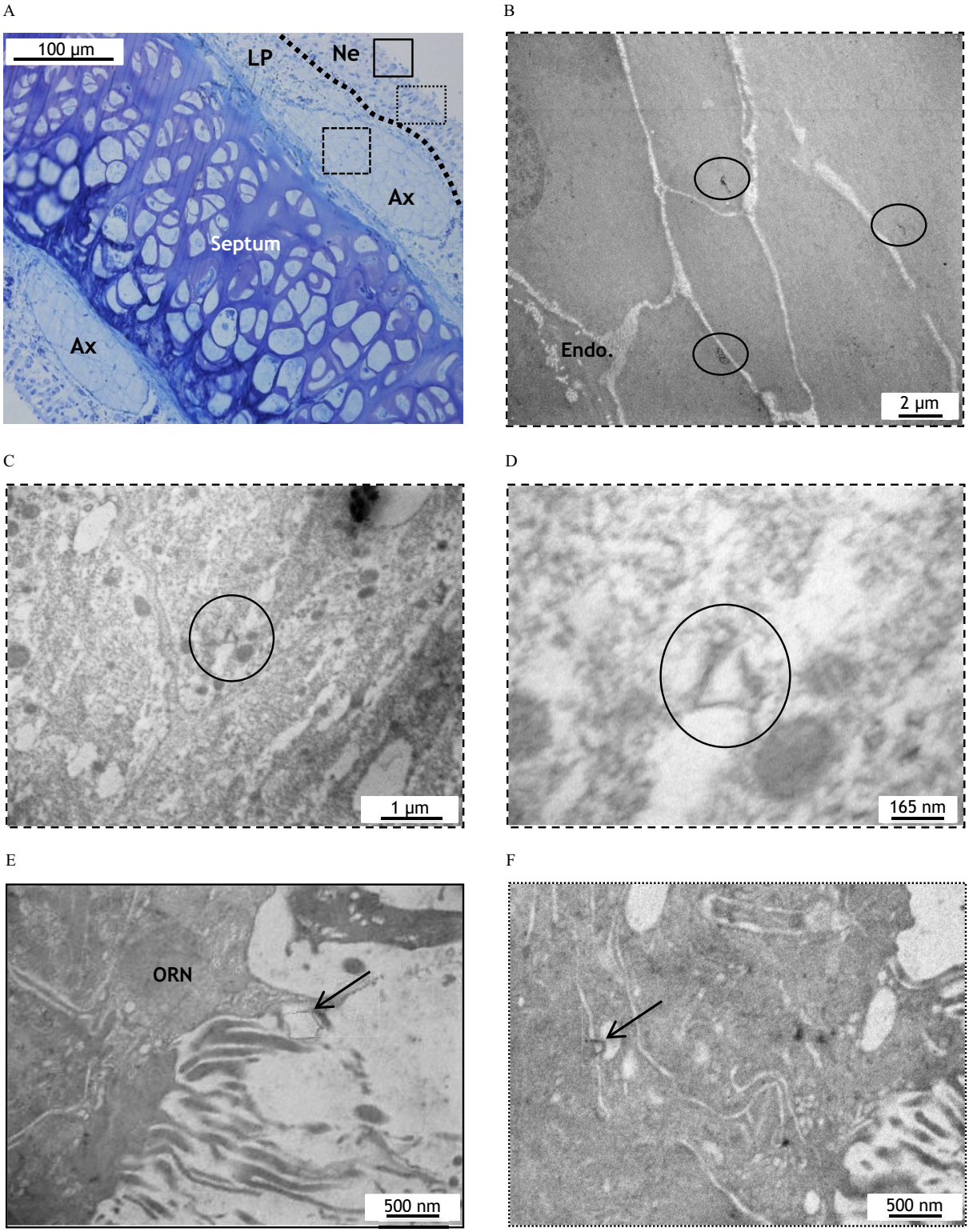

Figure 4. Optical toluidine blue and transmission electron microscopy (TEM) microphotographs of the olfactory mucosa. Results are presented for adult male Sprague-Dawley rats exposed to a uranium tetraoxide (UO_4) aerosol *via* inhalation, and samples were collected 4 h after the end of the exposure ($n = 6$ per group: one control group and two exposed groups, series 1 and 2). Analyses were performed as follows: two controls and three animals of series 2 were analyzed. For each animal, an average of 4 TEM grids with 2 to 3 sections on each grid were observed under the microscope, resulting in an average of 10 sections analyzed per animal. (A) Different areas are delineated with solid or dotted squares representing zones of TEM observations (scale bar: 100 µm). (B–D) TEM microphotographs showing electron-dense nanoparticles inside olfactory nerve bundles (circled) (scale bars: 2, 1, and 0.165 µm, respectively). These nanoscale objects tended to surround the axons rather than being inside them in the bundles. (E) TEM microphotograph representing the surface of the neuroepithelium with a particle in contact with olfactory receptor neuron (ORN) dendrites (scale bar: 500 nm). (F) An electron-dense particle detected in a paracellular junction of the neuroepithelium (scale bar: 500 nm). These observations are representative of exposed groups, as anatomical localization of electron-dense particles was similar in all sections analyzed for animals of series 2 (3/3 animals). Note: Ax, axon bundles; Endo., endoneurium; LP, lamina propria; Ne, neuroepithelium; ORN, olfactory receptor neuron.

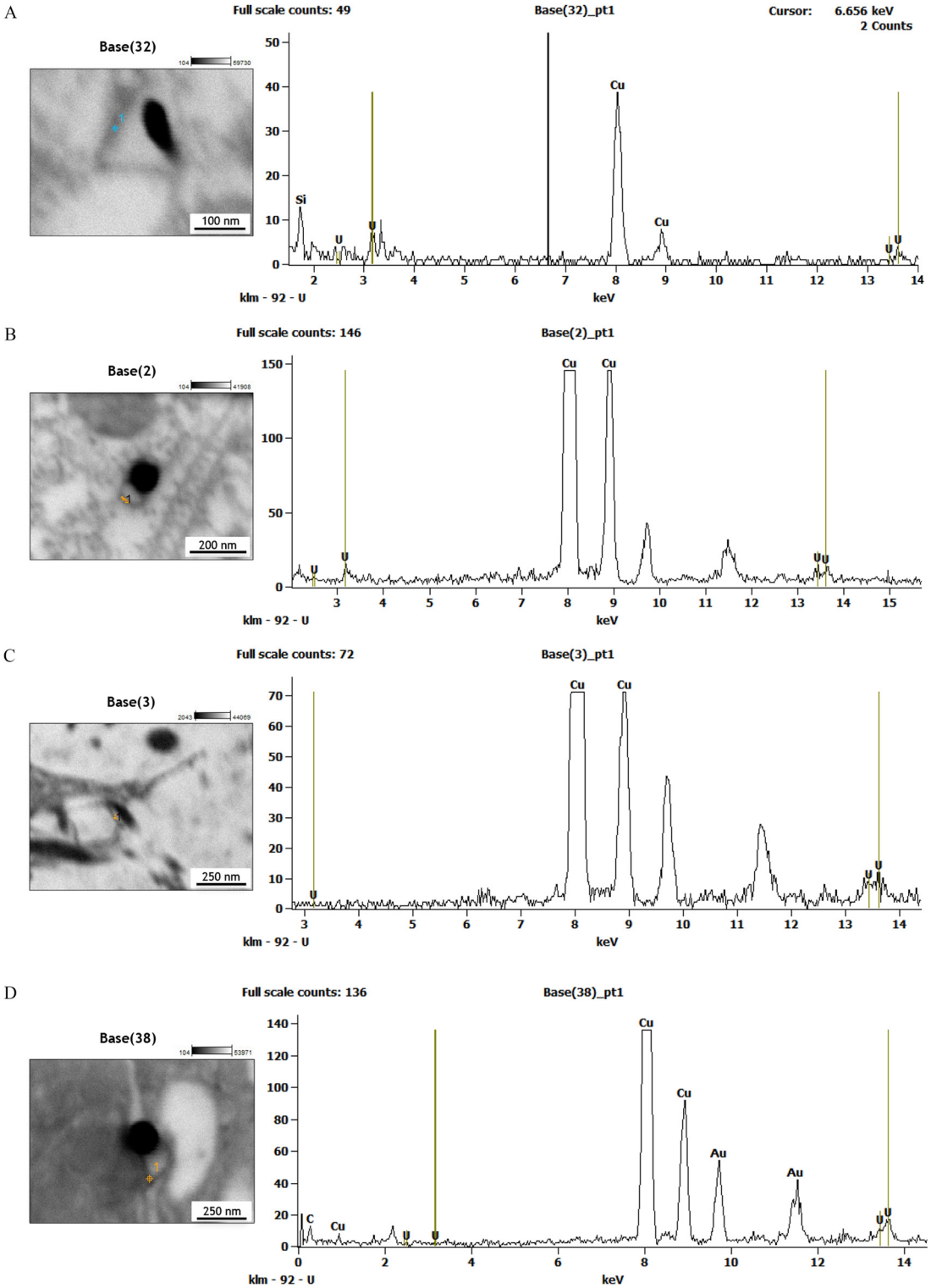

Figure 5. Scanning transmission electron microscopy (STEM) microphotographs associated with energy-dispersive X-ray spectroscopy (EDX) spectra: chemical elemental characterization of the electron-dense particles observed in different areas of the olfactory mucosa. Results are presented for adult male Sprague-Dawley rats exposed to a uranium tetraoxide (UO_4) aerosol *via* inhalation, and samples were collected 4 h after the end of the exposure ($n = 6$ per group: control group and two exposed groups, series 1 and 2). (A,B) In olfactory nerve bundles; (C) in olfactory receptor neuron dendrites; (D) in paracellular junctions (scale bars: 100, 200, 250, and 250 nm, respectively). The EDX analysis was performed in pointing shot mode as revealed by the mark resulting from the electron beam. Specific uranium energies were revealed for each selected particle for M and Lα at 3.1 and 13.6 KeV, demonstrating that the nanoparticles detected contained elemental uranium. Results are representative of exposed groups for animals from series 2.

Scanning Transmission Electron Microscopy (STEM) microphotographs of particles inside axon bundles (Figures 5A,B), in contact with ORN dendrites (Figure 5C) and in paracellular junctions (Figure 5D), are associated with their respective EDX spectra. The EDX analysis was performed in pointing shot mode as revealed by the mark resulting from the electron beam. Specific uranium energies were revealed for each selected particle for M and Lα at 3.1 and 13.6 KeV, demonstrating that the nanoparticles detected contained elemental uranium. Results are representative of exposed groups for animals from series 2.

Discussion

This study focuses on the mechanisms involved in the transport of uranium particles to the brain after exposure *via* inhalation in a rat model. The aim was to understand how metal particles can be directly translocated to the brain, which seems to be a direct target of exposure of particulate contaminants (Lucchini et al. 2012). This raises questions about the impact of exposure to inhaled compounds on cerebral functions (Heusinkveld et al. 2016).

Biokinetic studies were performed in order to study the distribution of several metals after inhalation in body organs including the brain. Contradictory observations have been reported regarding the ability of titanium dioxide nanoparticles to translocate to the brain (Gaté et al. 2017; Pujalté et al. 2017). On the other hand, translocation of lead oxide nanoparticles was observed in mouse brain after inhalation (Dumková et al. 2017), and silver nanoparticles were also translocated after intranasal instillation (Davenport et al. 2015). In addition to systemic biodistribution, the existence of transport *via* the olfactory pathway has been proposed for different particulate elements. Among the numerous examples in the literature are carbon (Oberdörster et al. 2004), manganese (Elder et al. 2006), ferric oxide (Wang et al. 2011), and silver nanoparticles (Wen et al. 2016), even though this direct transfer can differ according to their physicochemical form, as for aluminum oxide, for instance (Chalansonnet et al. 2018).

Adverse effects in relationship to the inhalation mode of contamination raise concerns in the nuclear field, as internal contamination is mainly caused by aerosols and is a potential health risk for exposed workers (Anderson et al. 2016; Samson et al. 2016). Previous studies have focused on the mechanisms of transport of uranium to the brain after upper airways contamination in a rat model (Tournier et al. 2009). Results presented in this study complement our previous observations demonstrating elemental uranium transport along olfactory nerve bundles after intranasal instillation in adult male rats (Ibanez et al. 2014). The question was then raised about transport after inhalation of particulate uranium as an aerosol. In the current study, adult male rats were exposed acutely to a polydisperse aerosol of UO_4 particles using the nose-only inhalation chamber. Four hours after exposure, uranium concentrations were measured by ICP-MS in selected brain structures along the anteroposterior axis. Results showed significantly higher uranium concentrations in all brain structures from exposed animals compared with their anatomically equivalent control structure. In addition, we observed an anteroposterior gradient in cerebral uranium concentration, with a typical accumulation of the contaminant in the olfactory bulbs, which is characteristic of direct nose-to-brain transfer of inhaled compounds. We also reproduced results obtained in previous uranium inhalation studies (Monleau et al. 2005; Tournier et al. 2009) and with our instillation model (Ibanez et al. 2014), which strengthens the assumption of uranium olfactory transport. Interestingly, OB, FC, and HIP uranium concentrations from series 1 and 2 were not statistically different, but we observed that uranium concentrations were significantly higher in Cer and BS from series 2 compared with series 1. This suggests that higher exposure concentrations lead to accelerated uranium translocation to posterior brain structures.

We then used SIMS microscopy in tissue sections of the olfactory epithelium to obtain robust anatomical localization of uranium in the olfactory system after inhalation. Results demonstrated a partial uranium localization at the surface of the neuroepithelium. Uranium was not detected or was below the detection limit of the SIMS technology in the lamina propria and olfactory nerve bundles layer. We thus hypothesized that we could have distinct physicochemical forms of uranium once in contact with biological tissues. For that reason, we performed TEM observations combined with EDX analysis that demonstrated the presence of nanoparticles containing uranium in precise anatomical areas of the OE: olfactory nerve bundles, olfactory receptor neuron dendrites, and paracellular junctions of the neuroepithelial cell. These observations, combined with the ICP-MS measurements that showed a uranium anteroposterior gradient, are coherent with direct transfer to the brain *via* the olfactory nerve. Altogether, the results strengthen our hypothesis of the coexistence of two distinct physicochemical forms of uranium and illustrate the complementarity of SIMS and TEM microscopy. It appears that uranium detected by SIMS microscopy on the neuroepithelial surface corresponds to a solubilized form 4 h after exposure, which is not detected using TEM. Indeed, uranium tetroxide is considered a type F oxide, meaning fast soluble (ICRP 1994). On the other hand, TEM, because it adds detection on a nanoscale, provides information on the *in situ* localization of elemental uranium as nanoparticles. Nanoparticles under the size of 500 nm were not detected using SIMS microscopy, even though they were present on the tissue sections, due to the size detection limit of this technology. Results from particle number distribution analysis can explain their origin, as our UO_4 aerosol is polydisperse, and there is a substantial proportion of particles of sizes below 500 nm (more than half of the population). Moreover, because we did not observe micron-size particles in either SIMS or TEM analysis, we used Poisson distribution to estimate the probability of detection of UO_4 particles in the analyzed tissue volume of the olfactory mucosa. Statistical analysis revealed that we had a probability of 62.1% of finding one or more 0.5-µm-diameter particles in the total volume of slices analyzed. In consequence, we cannot exclude that there might be micron-size particles in our neuroepithelial tissue and that they could also be translocated to the brain. Taken together, these results show the importance of combining different analytical approaches for anatomical detection of particulate contaminants *in vivo* after inhalation.

In humans, exogenous particles, such as magnetite particles, were observed in postmortem brain samples from 38 individuals (Maher et al. 2016). In previous experimental studies, the link between the external source of particulate pollutants and their presence in the central nervous system *via* the nose-to-brain connection was mainly demonstrated using ICP-MS measurements, autoradiography within the olfactory bulbs, or detection of fluorescent markers, particularly for mercury (Henriksson and Tjalve 1998), cobalt (Persson et al. 2003), and cadmium (Bondier et al. 2008). Maher et al. (2016) demonstrated the strength of combined techniques as they used magnetometry, high-resolution TEM, electron energy loss spectroscopy, and EDX analysis to examine the mineralogy, morphology, and composition of the magnetite nanoparticles. In our study, results obtained after inhalation exposure to UO_4 aerosol, combining SIMS and TEM-EDX analysis, confirmed that elemental uranium is directly translocated to the brain in an intranasally exposed rat model. We detected uranium in different physicochemical forms, solubilized or nanoparticulate, selectively detected by one or another technique. Final physicochemical forms were not studied, and this raises the question of

whether original UO_4 nanoparticles translocate or break down into other forms before translocation. Nevertheless, we can formulate the hypothesis that the property of undergoing such physicochemical changes is not unique to uranium. This could be a characteristic common to other metal nanoparticles: silver (Davenport et al. 2015), lead (Dumková et al. 2017), manganese (Elder et al. 2006), and iron particles (Wang et al. 2011), as suggested previously. In those studies, the authors provide strong evidence of direct translocation of these particles. In most studies, TEM was used to detect particles *in situ*, but no solubilized chemical elements were detected in tissues. Nevertheless, our solubilization hypothesis is supported by Wang et al. (2011), who studied microdistribution mapping of iron in the rat brain after nanoparticle intranasal exposure by synchrotron radiation microbeam X-ray fluorescence.

To our knowledge, ours is the first demonstration that elemental uranium can be transferred directly to the brain after aerosol inhalation in a rat model. This represents a potential hazard for workers exposed in the context of specific tasks that can lead to aerosol resuspension or direct emission in normal operating conditions of nuclear activities. It raises questions, in terms of radioprotection, since biokinetic models of contamination *via* inhalation do not take into account potential direct transfer of uranium to the brain *via* the olfactory pathway. In experimental models, rats exposed to repeated uranium inhalation demonstrated decreased performances in spatial working memory tests (Monleau et al. 2005). These experiments might reveal a cognitive impact of inhalation of aerosolized uranium. The literature provides guidance regarding investigation of the consequences of uranium translocation to the brain, since other metals have been shown to have deleterious effects on the brain after exposure via inhalation. It is widely observed that neuroinflammation is a key process in the mediation of the deleterious effects of particulate pollutants (Jayaraj et al. 2017). In 2011, Levesque et al. observed microglial cell activation and increased levels of proinflammatory cytokines (interleukin 6 and tumor necrosis factor-α) in the brains of rats exposed to diesel exhaust (DE) and diesel nanoparticles (Levesque et al. 2011). Very recently, the direct mediation of the adverse effect of DE inhalation *via* neuroinflammation was demonstrated in mouse brain neurogenic zones by use of pioglitazone pretreatment to prevent from the impairment of neurogenesis induced by DE in the subgranular zone (Coburn et al. 2018). Neuroinflammation is not exclusive to diesel particles. A recent study showed that inhalation of titanium dioxide nanoparticles induced age-dependent alteration of the blood-brain barrier in rats, which was associated with increased expression of proinflammatory cytokines (Disdier et al. 2017). These studies present neuroinflammation as a trigger of a negative impact on the brain.

In association with speciation studies, future areas of investigation focusing on these target processes should be developed in experimental paradigms of UO_4 aerosol inhalation, taking into account translocation of different physicochemical forms of uranium to the brain.

Acknowledgments

We thank Dr. C. Djediat, who runs the Transmission Electron Microscopy Platform at the Muséum National d'Histoire Naturelle, Plateau Technique de Microscopie Électronique et de Microanalyses (Paris, France), Dr. P. Beaunier [Université Pierre et Marie Curie, Service de Microscopie Electronique (IMPC), Paris], and Dr. D. Langui (Plateforme d'Imagerie Cellulaire Pitié-Salpêtrière, Institut du Cerveau et de la Moelle Epinière, Paris) for their expertise in electron microscopy. We wish to thank K. Chounlamountry for her valuable contribution to this project. F. Voyer is acknowledged for his assistance in animal care. This work was supported by the Institut de Radioprotection et de Sûreté Nucléaire (IRSN).

References

Anderson JL, Apostoaei AI, Yiin JH, Fleming DA, Tseng CY, Chen PH. 2016. Internal exposure to uranium in a pooled cohort of gaseous diffusion plant workers. Radiat Prot Dosimetry 168(4):471–477, PMID: 26113578, https://doi.org/10.1093/rpd/ncv357.

Block ML, Calderón-Garcidueñas L. 2009. Air pollution: mechanisms of neuroinflammation and CNS disease. Trends Neurosci 32(9):506–516, PMID: 19716187, https://doi.org/10.1016/j.tins.2009.05.009.

Bolton JL, Marinero S, Hassanzadeh T, Natesan D, Le D, Belliveau C, et al. 2017. Gestational exposure to air pollution alters cortical volume, microglial morphology, and microglia-neuron interactions in a sex-specific manner. Front Synaptic Neurosci 9:10, PMID: 28620294, https://doi.org/10.3389/fnsyn.2017.00010.

Bondier JR, Michel G, Propper A, Badot PM. 2008. Harmful effects of cadmium on olfactory system in mice. Inhal Toxicol 20(13):1169–1177, PMID: 18951233, https://doi.org/10.1080/08958370802207292.

Calderón-Garcidueñas L, Mora-Tiscareño A, Ontiveros E, Gómez-Garza G, Barragán-Mejía G, Broadway J, et al. 2008. Air pollution, cognitive deficits and brain abnormalities: a pilot study with children and dogs. Brain Cogn 68(2):117–127, PMID: 18550243, https://doi.org/10.1016/j.bandc.2008.04.008.

Calderón-Garcidueñas L, Reynoso-Robles R, Vargas-Martinez J, Gómez-Maqueo-Chew A, Pérez-Guillé B, Mukherjee PS, et al. 2016. Prefrontal white matter pathology in air pollution exposed Mexico City young urbanites and their potential impact on neurovascular unit dysfunction and the development of Alzheimer's disease. Environ Res 146:404–417, PMID: 26829765, https://doi.org/10.1016/j.envres.2015.12.031.

Chae N, Lee MH, Choi S, Park B, Song JS. 2019. Aerodynamic diameter and radioactivity distributions of radioactive aerosols from activated metals cutting for nuclear power plant decommissioning. J Hazard Mater 369:727–745, PMID: 30831525, https://doi.org/10.1016/j.jhazmat.2019.02.093.

Chalansonnet M, Carabin N, Boucard S, Merlen L, Melczer M, Antoine G, et al. 2018. Study of potential transfer of aluminum to the brain via the olfactory pathway. Toxicol Lett 283:77–85, PMID: 29180288, https://doi.org/10.1016/j.toxlet.2017.11.027.

Cheng L, Lau WKW, Fung TKH, Lau BWM, Chau BKH, Liang Y, et al. 2017. $PM_{2.5}$ exposure suppresses dendritic maturation in subgranular zone in aged rats. Neurotox Res 32(1):50–57, PMID: 28275902, https://doi.org/10.1007/s12640-017-9710-4.

Coburn JL, Cole TB, Dao KT, Costa LG. 2018. Acute exposure to diesel exhaust impairs adult neurogenesis in mice: prominence in males and protective effect of pioglitazone. Arch Toxicol 92(5):1815–1829, PMID: 29523932, https://doi.org/10.1007/s00204-018-2180-5.

Davenport LL, Hsieh H, Eppert BL, Carreira VS, Krishan M, Ingle T, et al. 2015. Systemic and behavioral effects of intranasal administration of silver nanoparticles. Neurotoxicol Teratol 51:68–76, PMID: 26340819, https://doi.org/10.1016/j.ntt.2015.08.006.

Dekkers S, Ma-Hock L, Lynch I, Russ M, Miller MR, Schins RPF, et al. 2018. Differences in the toxicity of cerium dioxide nanomaterials after inhalation can be explained by lung deposition, animal species and nanoforms. Inhal Toxicol 30(7–8):273–286, PMID: 30286672, https://doi.org/10.1080/08958378.2018.1516834.

Disdier C, Chalansonnet M, Gagnaire F, Gate L, Cosnier F, Devoy J, et al. 2017. Brain inflammation, blood brain barrier dysfunction and neuronal synaptophysin decrease after inhalation exposure to titanium dioxide nano-aerosol in aging rats. Sci Rep 7(1):12196, PMID: 28939873, https://doi.org/10.1038/s41598-017-12404-5.

Dumková J, Smutná T, Vrlíková L, Le Coustumer P, Večeřa Z, Dočekal B, et al. 2017. Sub-chronic inhalation of lead oxide nanoparticles revealed their broad distribution and tissue-specific subcellular localization in target organs. Part Fibre Toxicol 14(1):55, PMID: 29268755, https://doi.org/10.1186/s12989-017-0236-y.

Elder A, Gelein R, Silva V, Feikert T, Opanashuk L, Carter J, et al. 2006. Translocation of inhaled ultrafine manganese oxide particles to the central nervous system. Environ Health Perspect 114(8):1172–1178, PMID: 16882521, https://doi.org/10.1289/ehp.9030.

Gaté L, Disdier C, Cosnier F, Gagnaire F, Devoy J, Saba W, et al. 2017. Biopersistence and translocation to extrapulmonary organs of titanium dioxide nanoparticles after subacute inhalation exposure to aerosol in adult and elderly rats. Toxicol Lett 265:61–69, PMID: 27865850, https://doi.org/10.1016/j.toxlet.2016.11.009.

Henriksson J, Tjalve H. 1998. Uptake of inorganic mercury in the olfactory bulbs via olfactory pathways in rats. Environ Res 77(2):130–140, PMID: 9600806, https://doi.org/10.1006/enrs.1997.3817.

Heusinkveld HJ, Wahle T, Campbell A, Westerink RHS, Tran L, Johnston H, et al. 2016. Neurodegenerative and neurological disorders by small inhaled particles. Neurotoxicology 56:94–106, PMID: 27448464, https://doi.org/10.1016/j.neuro.2016.07.007.

Ibanez C, Suhard D, Tessier C, Delissen O, Lestaevel P, Dublineau I, et al. 2014. Intranasal exposure to uranium results in direct transfer to the brain along olfactory nerve bundles. Neuropathol Appl Neurobiol 40(4):477–488, PMID: 23672198, https://doi.org/10.1111/nan.12061.

ICRP (International Commission on Radiological Protection). 1994. Human respiratory tract model for radiological protection. A report of a Task Group of the International Commission on Radiological Protection. Ann ICRP 24(1–3):1–482, PMID: 7726471.

Jayaraj RL, Rodriguez EA, Wang Y, Block ML. 2017. Outdoor ambient air pollution and neurodegenerative diseases: the neuroinflammation hypothesis. Curr Environ Health Rep 4(2):166–179, PMID: 28444645, https://doi.org/10.1007/s40572-017-0142-3.

Levesque S, Taetzsch T, Lull ME, Kodavanti U, Stadler K, Wagner A, et al. 2011. Diesel exhaust activates and primes microglia: air pollution, neuroinflammation, and regulation of dopaminergic neurotoxicity. Environ Health Perspect 119(8):1149–1155, PMID: 21561831, https://doi.org/10.1289/ehp.1002986.

Lucchini RG, Dorman DC, Elder A, Veronesi B. 2012. Neurological impacts from inhalation of pollutants and the nose-brain connection. Neurotoxicology 33(4):838–841, PMID: 22178536, https://doi.org/10.1016/j.neuro.2011.12.001.

Maher BA, Ahmed IA, Karloukovski V, MacLaren DA, Foulds PG, Allsop D, et al. 2016. Magnetite pollution nanoparticles in the human brain. Proc Natl Acad Sci USA 113(39):10797–10801, PMID: 27601646, https://doi.org/10.1073/pnas.1605941113.

Monleau M, Bussy C, Lestaevel P, Houpert P, Paquet F, Chazel V. 2005. Bioaccumulation and behavioural effects of depleted uranium in rats exposed to repeated inhalations. Neurosci Lett 390(1):31–36, PMID: 16115730, https://doi.org/10.1016/j.neulet.2005.07.051.

Oberdörster G, Elder A, Rinderknecht A. 2009. Nanoparticles and the brain: cause for concern? J Nanosci Nanotechnol 9(8):4996–5007, PMID: 19928180, https://doi.org/10.1166/jnn.2009.gr02.

Oberdörster G, Sharp Z, Atudorei V, Elder A, Gelein R, Kreyling W, et al. 2004. Translocation of inhaled ultrafine particles to the brain. Inhal Toxicol 16(6–7):437–445, PMID: 15204759, https://doi.org/10.1080/08958370490439597.

Oudin A, Forsberg B, Adolfsson AN, Lind N, Modig L, Nordin M, et al. 2016. Traffic-related air pollution and dementia incidence in Northern Sweden: a longitudinal study. Environ Health Perspect 124(3):306–312, PMID: 26305859, https://doi.org/10.1289/ehp.1408322.

Peillon S, Fauvel S, Chagnot C, Gensdarmes F. 2017. Aerosol characterization and particle scrubbing efficiency of underwater operations during laser cutting of steel components for dismantling of nuclear facilities. Aerosol Air Qual Res 17(6):1463– 1373, https://doi.org/10.4209/aaqr.2016.09.0421.

Persson E, Henriksson J, Tjalve H. 2003. Uptake of cobalt from the nasal mucosa into the brain via olfactory pathways in rats. Toxicol Lett 145(1):19–27, PMID: 12962970, https://doi.org/10.1016/s0378-4274(03)00266-2.

Petitot F, Lestaevel P, Tourlonias E, Mazzucco C, Jacquinot S, Dhieux B, et al. 2013. Inhalation of uranium nanoparticles: respiratory tract deposition and translocation to secondary target organs in rats. Toxicol Lett 217(3):217–225, PMID: 23296105, https://doi.org/10.1016/j.toxlet.2012.12.022.

Pujalté I, Dieme D, Haddad S, Serventi AM, Bouchard M. 2017. Toxicokinetics of titanium dioxide (TiO2) nanoparticles after inhalation in rats. Toxicol Lett 265:77–85, PMID: 27884615, https://doi.org/10.1016/j.toxlet.2016.11.014.

Samson E, Piot I, Zhivin S, Richardson DB, Laroche P, Serond AP, et al. 2016. Cancer and non-cancer mortality among French uranium cycle workers: the TRACY cohort. BMJ Open 6(4):e010316, PMID: 27048635, https://doi.org/10.1136/bmjopen-2015-010316.

Tournier BB, Frelon S, Tourlonias E, Agez L, Delissen O, Dublineau I, et al. 2009. Role of the olfactory receptor neurons in the direct transport of inhaled uranium to the rat brain. Toxicol Lett 190(1):66–73, PMID: 19501638, https://doi.org/10.1016/j.toxlet.2009.05.022.

Wang Y, Wang B, Zhu MT, Li M, Wang HJ, Wang M, et al. 2011. Microglial activation, recruitment and phagocytosis as linked phenomena in ferric oxide nanoparticle exposure. Toxicol Lett 205(1):26–37, PMID: 21596115, https://doi.org/10.1016/j.toxlet.2011.05.001.

Wen R, Yang X, Hu L, Sun C, Zhou Q, Jiang G. 2016. Brain-targeted distribution and high retention of silver by chronic intranasal instillation of silver nanoparticles and ions in Sprague-Dawley rats. J Appl Toxicol 36(3):445–453, PMID: 26584724, https://doi.org/10.1002/jat.3260.

Woodward NC, Pakbin P, Saffari A, Shirmohammadi F, Haghani A, Sioutas C, et al. 2017. Traffic-related air pollution impact on mouse brain accelerates myelin and neuritic aging changes with specificity for CA1 neurons. Neurobiol Aging 53:48–58, PMID: 28212893, https://doi.org/10.1016/j.neurobiolaging.2017.01.007.